Journal Pre-proof

A two-scale framework for coupled mechanics-diffusion-reaction processes

Michael Poluektov, Łukasz Figiel

PII: S0020-7683(23)00283-4
DOI: https://doi.org/10.1016/j.ijsolstr.2023.112386
Reference: SAS 112386

To appear in: *International Journal of Solids and Structures*

Received date : 3 March 2023
Revised date : 16 May 2023
Accepted date : 9 June 2023

Please cite this article as: M. Poluektov and Łu. Figiel, A two-scale framework for coupled mechanics-diffusion-reaction processes. *International Journal of Solids and Structures* (2023), doi: https://doi.org/10.1016/j.ijsolstr.2023.112386.

A two-scale framework for coupled mechanics-diffusion-reaction processes

Michael Poluektov[1,2,4] and Łukasz Figiel[2,3]

[1]Department of Mathematics, School of Science and Engineering, University of Dundee, Dundee DD1 4HN, UK
[2]IINM, WMG, University of Warwick, Coventry CV4 7AL, UK
[3]Warwick Centre for Predictive Modelling, University of Warwick, Coventry CV4 7AL, UK
[4]Corresponding author, telephone: +447584824047, email: mpoluektov001@dundee.ac.uk

DRAFT: May 16, 2023

Abstract

There is a wide range of industrially-relevant problems where mechanical stresses directly affect kinetics of chemical reactions. For example, this includes formation of oxide layers on parts of micro-electro-mechanical systems (MEMS) and lithiation of Si in Li-ion batteries. Detailed understanding of these processes requires thermodynamically-consistent theories describing the coupled thermo-chemo-mechanical behaviour of those systems. Furthermore, as the majority of materials used in those systems have complex microstructures, multiscale modelling techniques are required for efficient simulation of their behaviour. Hence, the purpose of the present paper is two-fold: (1) to derive a thermodynamically-consistent thermo-chemo-mechanical theory; and (2) to propose a two-scale modelling approach based on the concept of computational homogenisation for the considered theory. The theory and the two-scale computational approach are implemented and tested using a number of computational examples, including the case of the reaction locking due to mechanical stresses.
Keywords: chemo-mechanics; stress-affected reactions; stress-affected diffusion; chemical affinity; reaction locking; computational homogenisation; cut-element method.

1 Introduction

Chemo-mechanics has been an emerging field that is highly relevant for understanding of the influence of mechanical stresses on the kinetics of chemical reactions in a variety of industrially-relevant problems [1–4]. This field focuses on developing theoretical frameworks and computational approaches that are able to describe temperature-dependent chemo-mechanical processes that can also be possibly coupled with other physical phenomena such as electrical processes in advanced materials.

It is well-known that mechanical stresses can affect the rates of chemical reactions [5]. Furthermore, some reactions require a certain critical value of normal stress to be achieved before a reaction on a surface can even start [6]. Mechanical forces can alter potential energy surfaces dynamically, giving access to products unavailable by traditional reaction pathways, which led to new developments in many fields, for example, in polymer science [7,8]. A recent overview of the field of mechanochemistry from the materials science point of view can be found in [9].

The influence of stresses on the reaction kinetics is modelled in various ways and at various scales. At the electronic structure scale, there are theories accounting for the significant effect of mechanical stresses on the activation barriers of chemical reactions, e.g. [10,11]. Such theories have common elements with the ones developed for calculating energy barriers in stress-driven solid-solid phase transitions [12]. At the atomistic scale, idealised models are used to derive approximate relations between the mechanical forces and rate constants of the reactions, e.g. [13]. At the macroscopic scale, various phenomenological models are typically used, e.g. [14, 15].

From the continuum mechanics point of view, chemical reactions in solids have long been modelled as source/sink terms in the mass balance equation for the diffusive species [16]. Within this field, some research works focus primarily on mechano-diffusion and the effect of mechanical stresses on the kinetics of the transport processes, without accounting for the source/sink terms in the mass balance, e.g. [17–20]. Other research works consider mechanics-diffusion-reaction as three coupled processes and make a distinction between the stress-affected volumetric reactions, e.g. [21–23], and the stress-affected localised reactions, e.g. [24–26].

The localised reactions take place at a propagating interface between the chemically transformed and untransformed phases, and the gaseous-type reactant, which is inserted into the solid, diffuses through the transformed phase and it is consumed by the chemical reaction at the interface. A recent overview of chemo-mechanical theories covering localised reactions in solids can be found in [27]. There are also works where both volumetric and localised reactions are modelled simultaneously; for example, in [28], growth of an oxide layer (Cr_2O_3) on a Cr-Fe alloy is modelled, accounting for the propagation of the oxide-metal interface, at which Cr ions are split from the alloy, and for the chemical reaction between Cr and O inside the volume of the oxide layer.

When the volumetric reactions are considered, different terminology is used across the literature. The atoms of the gaseous-type reactant can also be referred to as mobile and trapped/immobile [23], with trapping/immobilisation of the atoms corresponding to the chemical reaction. However, the same equations are considered — the mass balance with the volumetric source/sink term. The most recent general thermo-chemo-mechanical theory that includes the separation between the the diffusion and the volumetric reaction processes can be found in [29].

As the majority of advanced materials undergoing the above chemo-mechanical processes are highly heterogeneous with complex hierarchical microstructures/morphologies, efficient predictive modelling techniques require a multiscale approach. One such established technique is computational homogenisation [30, 31]. It was initially developed to capture the mechanical behaviour of advanced materials across micro and macro scales, and was subsequently extended to other processes, such as thermal [32] and thermo-mechanical [33]. Development of this technique for chemo-mechanical or electro-chemo-mechanical problems presents its own challenges, in particular, handling of the diffusion and the reaction processes, with their numerical implementation within the finite-strain framework. Some developments have been proposed for coupled electro-chemo-mechanics, but either without the explicit modelling of the reaction process [34, 35], or with accounting for it, but within the small-strain framework [36]. The most recent computational homogenisation theories for the diffusion process can be found in [37] and for coupled mechanics-diffusion in [38, 39].

The present paper aims to achieve a two-fold objective: (1) to derive a general thermo-chemo-mechanical theory directly from the thermodynamics framework of continuum mechanics (i.e with the fewest possible number of assumptions), following the concept of separation of the diffusion and the reaction processes; and (2) to propose a two-scale approach for the theory with its computational treatment. The entire proposed modelling framework is implemented numerically using the recently-developed CutFEM approach and tested using a number of computational examples, including the demonstration of the reaction locking due to mechanical stresses.

2 Theory

2.1 Balance laws

The starting point for obtaining the set of governing equations are the balance laws and the dissipation inequality, written for the open system consisting of the deformable solid and the gaseous-type constituent (will be referred to as 'gas') diffusing through the solid and reacting with it, as illustrated in figure 1. The standard solid mechanics approach is employed, where the current and the reference configurations are considered. The balance laws are written with respect to the reference configuration of the body. The same tensor notation is used as in the previous publication by the authors, section 2 of reference [40]. Here, $\boldsymbol{F} = (\nabla_0 \vec{x})^{\mathrm{T}}$ is the deformation gradient, which maps the reference configuration to the current configuration, and $\vec{x}$ as the current position vector of a material point as a function of position vector $\vec{X}$ of the point in the reference configuration and time t. The displacement is denoted as $\vec{u} = \vec{x} - \vec{X}$.

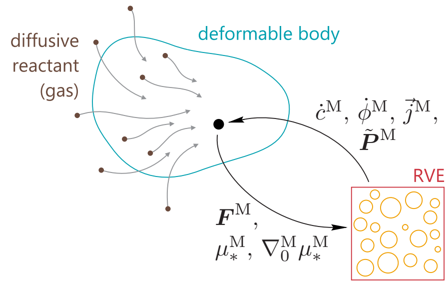

Figure 1: The schematic illustration of a chemo-mechanical problem with the two-scale split into the macroscopic domain and the RVE.

Nabla operator ∇_0 is defined with respect to the reference configuration. The volume change is denoted as $J = \det \boldsymbol{F}$.

Path-connected domain $\Omega \in \mathbb{R}^3$ in the reference configuration is considered. The gas is diffusing through the domain, hence its change of mass can be written as

$$\frac{\mathrm{d}}{\mathrm{d}t}\int_\Omega \rho_*^0 \,\mathrm{d}\Omega = -\int_\Gamma \vec{j}\cdot\vec{N}_\Gamma \,\mathrm{d}\Gamma + \frac{\mathrm{d}}{\mathrm{d}t}\int_\Omega \zeta\phi \,\mathrm{d}\Omega, \tag{1}$$

where ρ_*^0 is the mass density of the gas per unit volume of the reference configuration, $\vec{j}$ is the diffusive flux of the gas per unit surface in the reference configuration, $\Gamma = \partial\Omega$ is the boundary of domain Ω, vector $\vec{N}_\Gamma$ is the outward unit normal vector to Γ, and field $\phi \in [0, 1]$ is the extent of the reaction. Parameter ζ is the normalisation coefficient and it corresponds to the amount of mass of the gas per unit volume of the reference configuration produced within the entire reaction processes (i.e. from extent $\phi = 0$ to extent $\phi = 1$). Thus, in the case of the consumption of the gas during the reaction, ζ is negative. Diffusive flux $\vec{j}$ is by definition proportional to velocity $\vec{V}_*^0$ of the gas with respect to the points of the reference configuration, $\vec{j} = \rho_*^0\vec{V}_*^0$. The last term in equation (1) corresponds to the consumption of the gas due to the chemical reaction.

The change of the total linear momentum of the solid and the gas within domain Ω is

$$\frac{\mathrm{d}}{\mathrm{d}t}\int_\Omega \left(\rho^0\vec{v} + \rho_*^0\vec{v}_*\right)\mathrm{d}\Omega = \int_\Gamma \left(\boldsymbol{P} + \boldsymbol{P}_* - \vec{v}_*\vec{j}\right)\cdot\vec{N}_\Gamma \,\mathrm{d}\Gamma + \int_\Omega \left(\rho^0\vec{b} + \rho_*^0\vec{b}_*\right)\mathrm{d}\Omega, \tag{2}$$

where ρ^0 is the mass density of the solid per unit volume of the reference configuration, $\vec{v}$ and $\vec{v}_*$ are the velocities of the points of the solid and the gas, respectively, $\boldsymbol{P}$ and $\boldsymbol{P}_*$ are the first Piola-Kirchhoff stress tensors of the solid and the gas, respectively, $\vec{b}$ and $\vec{b}_*$ are the volumetric forces acting on the solid and the gas, respectively. The third term in the surface integral in equation (2) is the change of the momentum due to the influx of the gas through the boundary. In the current configuration, the Cauchy stress of the gas is hydrostatic. When transformed to the reference configuration, the resulting first Piola-Kirchhoff is $\boldsymbol{P}_* = -p_*J\boldsymbol{F}^{-\mathrm{T}}$, where p_* is the pressure of the gas.

The change of the total energy of the solid and the gas is

$$\begin{aligned}\frac{\mathrm{d}}{\mathrm{d}t}\int_\Omega \left(\rho^0 u + \rho_*^0 u_* + \frac{1}{2}\rho^0\vec{v}\cdot\vec{v} + \frac{1}{2}\rho_*^0\vec{v}_*\cdot\vec{v}_*\right)\mathrm{d}\Omega = \int_\Gamma \Big(\vec{v}\cdot\boldsymbol{P} + \vec{v}_*\cdot\boldsymbol{P}_* -\\ - u_*\vec{j} - \frac{1}{2}\vec{v}_*\cdot\vec{v}_*\vec{j} - \vec{h}\Big)\cdot\vec{N}_\Gamma \,\mathrm{d}\Gamma + \int_\Omega \left(\rho^0\vec{b}\cdot\vec{v} + \rho_*^0\vec{b}_*\cdot\vec{v}_* + \rho^0 r + \rho_*^0 r_*\right)\mathrm{d}\Omega,\end{aligned} \tag{3}$$

where u and u_* are the internal energies per unit of mass the solid and the gas, respectively, r and r_* are the internal heat sources per unit of mass of the solid and the gas, respectively, $\vec{h}$ is the heat flux. The surface integral in equation (3) consists of the rate of work of external load applied to the solid and the gas, and of the influx of the energy due to the diffusion. The energy itself consist of the internal energy and the kinetic energy.

Assuming that the solid and the gas are at the same temperature locally, the change of the entropy is

$$\frac{\mathrm{d}}{\mathrm{d}t}\int_\Omega \left(\rho^0 s + \rho_*^0 s_*\right)\mathrm{d}\Omega \geq -\int_\Gamma \left(\frac{1}{T}\vec{h} + s_*\vec{j}\right)\cdot\vec{N}_\Gamma \,\mathrm{d}\Gamma + \int_\Omega \frac{\rho^0 r + \rho_*^0 r_*}{T}\,\mathrm{d}\Omega, \tag{4}$$

where s and s_* are the entropies per unit of mass the solid and the gas, respectively, T is the temperature. Similarly to the previous equations, the surface integral contains the influx of entropy due to the diffusion.

After rewriting equations (1)-(4) in the differential form and performing substitutions (without any further assumptions), the system of the governing equations (consisting of the mass, the momentum and the energy balance equations) is obtained:

$$M_*\dot{c} = -\nabla_0 \cdot \vec{j} + \zeta\dot{\phi}, \tag{5}$$

$$\left(\rho^0 + M_* c\right)\dot{\vec{v}} + 2\dot{\boldsymbol{F}} \cdot \vec{j} + \boldsymbol{F} \cdot \dot{\vec{j}} + \zeta\dot{\phi}\vec{v} = \nabla_0 \cdot \left(\tilde{\boldsymbol{P}}^{\mathrm{T}} - \frac{\vec{j}\vec{j}}{M_* c} \cdot \boldsymbol{F}^{\mathrm{T}}\right) + \rho^0\vec{b} + M_* c\vec{b}_*, \tag{6}$$

$$T\dot{S} + \dot{T}S + \dot{f} = R - \nabla_0 \cdot \vec{H} - \frac{1}{M_*}\vec{j} \cdot \vec{q} + \dot{c}\mu_* + \tilde{\boldsymbol{P}}^{\mathrm{T}} : \dot{\boldsymbol{F}} + \dot{\phi}a, \tag{7}$$

where M_* is the molar masses of the gas, $c = \rho_*^0/M_*$ is the molar concentration of the gas per unit volume of the reference configuration, $\tilde{\boldsymbol{P}} = \boldsymbol{P} + \boldsymbol{P}_*$ is the total first Piola-Kirchhoff stress tensor, $S = \rho^0 s + \rho_*^0 s_*$ is the total entropy per unit volume of the reference configuration, $R = \rho^0 r + \rho_*^0 r_*$ is the total heat source per unit volume of the reference configuration, $\vec{H} = \vec{h} + s_* T\vec{j}$ is the total heat flux, $\mu_* = M_*\psi_* + p_* J/c$ is the chemical potential, $\psi = u - Ts$ and $\psi_* = u_* - Ts_*$ are the Helmholtz energies per unit of mass of the solid and of the gas, respectively, $f = \rho^0\psi + \rho_*^0\psi_*$ is the total Helmholtz energy per unit volume of the reference configuration, and quantities $\vec{q}$ and a are defined as

$$\vec{q} = \nabla_0\mu_* + \frac{1}{c}\boldsymbol{F}^{\mathrm{T}} \cdot \left(\nabla_0 \cdot \tilde{\boldsymbol{P}}^{\mathrm{T}} + \rho^0\vec{b} - \rho^0\dot{\vec{v}}\right), \tag{8}$$

$$a = -\frac{\mu_*\zeta}{M_*} + \frac{1}{2}\vec{v} \cdot \vec{v}\zeta + \frac{1}{2}\frac{\boldsymbol{C} : \vec{j}\vec{j}\zeta}{M_*^2 c^2} + \frac{\boldsymbol{F} : \vec{j}\vec{v}\zeta}{M_* c}, \tag{9}$$

where $\boldsymbol{C} = \boldsymbol{F}^{\mathrm{T}} \cdot \boldsymbol{F}$. The local form of the dissipation inequality becomes

$$-\dot{T}S - \dot{f} - \vec{H} \cdot \frac{\nabla_0 T}{T} - \frac{1}{M_*}\vec{j} \cdot \vec{q} + \dot{c}\mu_* + \tilde{\boldsymbol{P}}^{\mathrm{T}} : \dot{\boldsymbol{F}} + \dot{\phi}a \geq 0. \tag{10}$$

Now, the form of the dissipation inequality will facilitate writing the dependence of the thermodynamic fluxes as functions of the corresponding thermodynamic forces.

2.2 Choice of independent variables

To present the framework in the simplest possible way, the case of chemo-elasticity (non-linear finite-strain case) is considered. However, as will be shown below, the framework is generalisable for more complex non-linear materials' constitutive behaviour.

It is assumed that the total deformation gradient can be decomposed into the elastic and the non-mechanical parts:

$$\boldsymbol{F} = \boldsymbol{F}_{\mathrm{E}} \cdot \boldsymbol{F}_{\mathrm{C}}, \tag{11}$$

where $\boldsymbol{F}_{\mathrm{C}} = \boldsymbol{F}_{\mathrm{C}}(c, \phi, T)$. Now, variables $\boldsymbol{F}_{\mathrm{E}}$, c, ϕ, T can be taken to be independent and the Helmholtz energy density is assumed to be a function of these variables:

$$f = f\left(\boldsymbol{F}_{\mathrm{E}}, c, \phi, T\right). \tag{12}$$

This means that the time derivatives of f and $\boldsymbol{F}$ become the following:

$$\dot{f} = \frac{\partial f}{\partial \boldsymbol{F}_{\mathrm{E}}} : \dot{\boldsymbol{F}}_{\mathrm{E}}^{\mathrm{T}} + \frac{\partial f}{\partial c}\dot{c} + \frac{\partial f}{\partial \phi}\dot{\phi} + \frac{\partial f}{\partial T}\dot{T}, \tag{13}$$

$$\dot{\boldsymbol{F}} = \dot{\boldsymbol{F}}_{\mathrm{E}} \cdot \boldsymbol{F}_{\mathrm{C}} + \boldsymbol{F}_{\mathrm{E}} \cdot \frac{\partial \boldsymbol{F}_{\mathrm{C}}}{\partial c}\dot{c} + \boldsymbol{F}_{\mathrm{E}} \cdot \frac{\partial \boldsymbol{F}_{\mathrm{C}}}{\partial \phi}\dot{\phi} + \boldsymbol{F}_{\mathrm{E}} \cdot \frac{\partial \boldsymbol{F}_{\mathrm{C}}}{\partial T}\dot{T}. \tag{14}$$

In general, the Helmholtz energy density can also be a function of $\nabla_0\phi$ and other state variables, but this case is not considered in the present paper.

Equations (13)-(14) are substituted into equation (10). The resulting dissipation inequality should be fulfilled under various different thermodynamic paths. The standard way of enforcing this is requiring the multiplies, which are in front of the time derivatives of the independent variables that can change arbitrarily, to be zeros. This gives

$$\tilde{\boldsymbol{P}} = \frac{\partial f}{\partial \boldsymbol{F}_{\mathrm{E}}} \cdot \boldsymbol{F}_{\mathrm{C}}^{-\mathrm{T}}, \tag{15}$$

$$S = -\frac{\partial f}{\partial T} + \tilde{\boldsymbol{P}}^{\mathrm{T}} : \left(\boldsymbol{F}_{\mathrm{E}} \cdot \frac{\partial \boldsymbol{F}_{\mathrm{C}}}{\partial T} \right), \tag{16}$$

$$\mu_* = \frac{\partial f}{\partial c} - \tilde{\boldsymbol{P}}^{\mathrm{T}} : \left(\boldsymbol{F}_{\mathrm{E}} \cdot \frac{\partial \boldsymbol{F}_{\mathrm{C}}}{\partial c} \right), \tag{17}$$

which correspond to multipliers in front of $\dot{\boldsymbol{F}}_{\mathrm{E}}$, $\dot{T}$ and $\dot{c}$, respectively. The dissipation inequality becomes the following:

$$-\vec{H} \cdot \frac{\nabla_0 T}{T} - \frac{1}{M_*} \vec{j} \cdot \vec{q} + A\dot{\phi} \geq 0, \tag{18}$$

where $\dot{\phi}$ has the physical meaning of the reaction rate and A is the chemical affinity:

$$A = -\frac{\mu_* \zeta}{M_*} - \frac{\partial f}{\partial \phi} + \tilde{\boldsymbol{P}}^{\mathrm{T}} : \left(\boldsymbol{F}_{\mathrm{E}} \cdot \frac{\partial \boldsymbol{F}_{\mathrm{C}}}{\partial \phi} \right) + \frac{1}{2} \vec{v} \cdot \vec{v} \zeta + \frac{1}{2} \frac{\boldsymbol{C} : \vec{j}\vec{j} \zeta}{M_*^2 c^2} + \frac{\boldsymbol{F} : \vec{j}\vec{v}\zeta}{M_* c}. \tag{19}$$

It should be mentioned that the way of obtaining dissipation inequality (18) is relatively standard for coupled problems in mechanics, and similar sequence of steps has been previously used to obtain an expression for the chemical affinity in chemo-mechanics [29]. However, in the present paper, the dynamic terms responsible for the inertial effects have not been neglected, hence, expression (19) also contains the dynamic terms, not present in the previous works.

To ensure that the entropy production due to the heat propagation and due to the gas diffusion are non-negative, the following constitutive laws can be enforced:

$$\vec{H} = -\boldsymbol{\Lambda} \cdot \frac{\nabla_0 T}{T}, \tag{20}$$

$$\vec{j} = -\frac{1}{M_*} \boldsymbol{K} \cdot \vec{q}, \tag{21}$$

where $\boldsymbol{\Lambda}$ and $\boldsymbol{K}$ are positive-definite tensors. The remaining part of the dissipation inequality corresponds to the entropy production due to the chemical reaction:

$$A\dot{\phi} \geq 0. \tag{22}$$

Equation (22) allows choosing a constitutive law for reaction rate ω as a function the driving force for the chemical reaction (the chemical affinity):

$$\dot{\phi} = \omega, \qquad \omega = \omega\,(A)\,. \tag{23}$$

Finally, it can be useful to substitute relations (13)-(17) and (19) into (7) and to obtain the following governing equation for the heat propagation:

$$T \frac{\partial S}{\partial T} \dot{T} = R - \nabla_0 \cdot \vec{H} + \boldsymbol{K}^{-1} : \vec{j}\vec{j} + \left(A - T \frac{\partial S}{\partial \phi} \right) \dot{\phi} - T \frac{\partial S}{\partial c} \dot{c} - T \frac{\partial S}{\partial \boldsymbol{F}_{\mathrm{E}}} : \dot{\boldsymbol{F}}_{\mathrm{E}}^{\mathrm{T}}, \tag{24}$$

where decomposition of $\dot{S}$ similar to equation (13) has been used.

2.2.1 Chemo-elasto-plasticity

If elasto-viscoplasticity is considered, the total deformation gradient can be decomposed into the elastic, the viscoplastic and the non-mechanical parts:

$$\boldsymbol{F} = \boldsymbol{F}_{\mathrm{E}} \cdot \boldsymbol{F}_{\mathrm{P}} \cdot \boldsymbol{F}_{\mathrm{C}}. \tag{25}$$

Substitution into equation (10) and splitting the result into a set of stronger inequalities leads to

$$\tilde{\boldsymbol{P}} = \frac{\partial f}{\partial \boldsymbol{F}_{\mathrm{E}}} \cdot \boldsymbol{F}_{\mathrm{P}}^{-\mathrm{T}} \cdot \boldsymbol{F}_{\mathrm{C}}^{-\mathrm{T}}, \tag{26}$$

$$\left(\boldsymbol{F}_{\mathrm{C}} \cdot \tilde{\boldsymbol{P}}^{\mathrm{T}} \cdot \boldsymbol{F}_{\mathrm{E}} \right) : \dot{\boldsymbol{F}}_{\mathrm{P}} \geq 0, \tag{27}$$

where the first equation replaces equation (15), giving an expression for the first Piola-Kirchhoff stress tensor, while the second equation is an additional inequality that should be used to write the evolution law for the plastic deformations. In particular, it is straightforward to rewrite inequality (27) using the objective tensors:

$$J\tilde{\boldsymbol{\sigma}} : \boldsymbol{D}_{\mathrm{P}} \geq 0, \tag{28}$$

where $\tilde{\boldsymbol{\sigma}} = J^{-1}\tilde{\boldsymbol{P}} \cdot \boldsymbol{F}^{\mathrm{T}}$ is the Cauchy stress and

$$\boldsymbol{D}_{\mathrm{P}} = \frac{1}{2}\left(\boldsymbol{L}_{\mathrm{P}} + \boldsymbol{L}_{\mathrm{P}}^{\mathrm{T}}\right), \qquad \boldsymbol{L}_{\mathrm{P}} = \boldsymbol{F}_{\mathrm{E}} \cdot \dot{\boldsymbol{F}}_{\mathrm{P}} \cdot \boldsymbol{F}_{\mathrm{P}}^{-1} \cdot \boldsymbol{F}_{\mathrm{E}}^{-1}.$$

Now, one can write an evolution law for $\boldsymbol{D}_{\mathrm{P}}$ as a function of $\tilde{\boldsymbol{\sigma}}$ that satisfies the inequality. It should also be noted that, in presence of $\boldsymbol{F}_{\mathrm{P}}$, equations (16), (17) and (19) will have an obvious change — tensor $\boldsymbol{F}_{\mathrm{E}}$ will be replaced by $\boldsymbol{F}_{\mathrm{E}} \cdot \boldsymbol{F}_{\mathrm{P}}$, while equation (24) will have an additional term

$$-T\frac{\partial S}{\partial \boldsymbol{F}_{\mathrm{P}}} : \dot{\boldsymbol{F}}_{\mathrm{P}}^{\mathrm{T}}$$

at the right-hand side. This section provides just an example of how inelasticity can be incorporated into the framework. From now onwards, for the purpose of the paper, it is sufficient to consider only chemo-elasticity.

2.3 Simplifications of the theoretical framework

2.3.1 Quasi-statics

In chemo-mechanics, it can be useful to distinguish the time scales of the mechanical and of the chemical processes. Typical chemical reaction times are much higher than the time scale of the inertial effects in solids. For example, 1 micrometre of Si nanowire undergoes reaction with Li in 50–100 seconds [41]. Therefore, the dynamical terms in the linear momentum balance can be neglected. More specifically, the first and the fourth terms of equation (6) that contain the acceleration and the velocity of the material points, respectively, are neglected. Assuming that the strain of the solid and the diffusive flux are changing relatively slowly, the second and the third terms of equation (6) that contain the time derivatives of $\boldsymbol{F}$ and $\vec{j}$, respectively, are also neglected. This leads to a quasi-static version of the linear momentum balance equation:

$$\nabla_0 \cdot \left(\tilde{\boldsymbol{P}}^{\mathrm{T}} - \frac{\vec{j}\vec{j}}{M_* c} \cdot \boldsymbol{F}^{\mathrm{T}}\right) + \rho^0\vec{b} + M_* c\vec{b}_* = \vec{0}. \tag{29}$$

Furthermore, the dynamical terms (containing $\vec{v}$) in the chemical affinity can also be neglected:

$$A = -\frac{\mu_*\zeta}{M_*} - \frac{\partial f}{\partial \phi} + \tilde{\boldsymbol{P}}^{\mathrm{T}} : \left(\boldsymbol{F}_{\mathrm{E}} \cdot \frac{\partial \boldsymbol{F}_{\mathrm{C}}}{\partial \phi}\right) + \frac{1}{2}\frac{\boldsymbol{C} : \vec{j}\vec{j}\zeta}{M_*^2 c^2}. \tag{30}$$

Similarly, terms with $\vec{v}$ and $\dot{\vec{v}}$ are neglected in equations (8)-(9).

2.3.2 Further assumptions

In order to perform the two-scale treatment of the governing equations, i.e. introduce two scales and couple them, two additional assumptions are introduced to facilitate handling of the equations. First, volumetric forces $\vec{b}$ and $\vec{b}_*$ acting on the solid and the gas, respectively, are neglected. Second, terms containing $\vec{j}\vec{j}$ in the linear momentum balance equation, the energy balance equation and the dissipation inequality have the dynamic nature, therefore, are assumed to be small compared to other terms. This leads to the following linear momentum balance equation:

$$\nabla_0 \cdot \tilde{\boldsymbol{P}}^{\mathrm{T}} = \vec{0}. \tag{31}$$

Consequently, variables $\vec{q}$ and a in equation (7) become

$$\vec{q} = \nabla_0 \mu_*, \tag{32}$$

$$a = -\frac{\mu_*\zeta}{M_*}, \tag{33}$$

and the chemical affinity reduces to

$$A = -\frac{\mu_*\zeta}{M_*} - \frac{\partial f}{\partial \phi} + \tilde{\boldsymbol{P}}^{\mathrm{T}} : \left(\boldsymbol{F}_{\mathrm{E}} \cdot \frac{\partial \boldsymbol{F}_{\mathrm{C}}}{\partial \phi}\right). \tag{34}$$

2.4 Two-scale treatment of mechanics-diffusion-reaction

Two different scales are considered: macroscopic and microscopic. Both scales are described with the same governing equations, introduced above. The scales are coupled — microscopic scale has macroscopic fields as boundary conditions, while constitutive laws at the macroscopic scale are obtained by averaging the microscopic scale quantities. The goal of this section is to summarise the micro-micro coupling.

It is sufficient to consider an isothermal macroscopic scale model. In this case, the problem simplifies, and only the mechanics-diffusion-reaction part must be treated in a two-scale way. There are already established techniques for performing computational homogenisation of the thermal part, e.g. [32, 33], and they can be separately added to the framework described in the present paper.

Following the assumptions of sections 2.3.1 and 2.3.2, the macroscopic governing equations can be written as:

$$M_*\dot{c}^{\mathrm{M}} = -\nabla_0^{\mathrm{M}} \cdot \vec{j}^{\mathrm{M}} + \zeta\dot{\phi}^{\mathrm{M}}, \tag{35}$$

$$\nabla_0^{\mathrm{M}} \cdot \left(\tilde{\boldsymbol{P}}^{\mathrm{M}}\right)^{\mathrm{T}} = \vec{0}, \tag{36}$$

where the equations have exactly the same structure as equations (5) and (31), but superscript 'M' is added to the quantities defined at the macroscopic scale. Furthermore, operator ∇_0^{M} is defined as differentiation with respect to position vector $\vec{X}^{\mathrm{M}}$ of the point of the macroscopic scale model in the reference configuration. The displacement at the macroscopic scale is denoted as $\vec{u}^{\mathrm{M}} = \vec{x}^{\mathrm{M}} - \vec{X}^{\mathrm{M}}$.

2.4.1 Macro to micro transition

The diffusion problem is considered first and the homogenisation of the diffusion is written similarly to [37], however, also accounting for the reaction. There is some freedom in selection of quantities for the two-scale coupling. As it will be evident later, choosing the chemical potential as such quantity leads to an energetically-consistent coupling. Therefore, the chemical potential at the microscopic scale is represented as

$$\mu_* = \mu_*^{\mathrm{M}} + \nabla_0^{\mathrm{M}}\mu_*^{\mathrm{M}} \cdot \left(\vec{X} - \vec{X}^{\mathrm{ref}}\right) + \mu_*^{\mathrm{f}}, \tag{37}$$

where μ_*^{M} is the macroscopic chemical potential (spatially-constant at the microscopic scale), $\vec{X}^{\mathrm{ref}}$ is some reference position vector, μ_*^{f} is the remaining (fluctuation) part of the chemical potential (spatially-inhomogeneous at the microscopic scale). Such representation allows writing the volume average of the gradient of the chemical potential:

$$\frac{1}{V_\Omega}\int_\Omega \nabla_0\mu_* \,\mathrm{d}\Omega = \nabla_0^{\mathrm{M}}\mu_*^{\mathrm{M}} + \frac{1}{V_\Omega}\int_\Omega \nabla_0\mu_*^{\mathrm{f}} \,\mathrm{d}\Omega = \nabla_0^{\mathrm{M}}\mu_*^{\mathrm{M}} + \frac{1}{V_\Omega}\int_\Gamma \vec{N}_\Gamma \mu_*^{\mathrm{f}} \,\mathrm{d}\Gamma, \tag{38}$$

where V_Ω is the volume of the microscopic domain.

The macro to micro transition is now performed by demanding the consistency between the volume-averaged microscopic and the macroscopic chemical potential gradients. To have such consistency, the fluctuation part of the chemical potential is assumed to be zero at the boundary of the RVE:

$$\mu_*^{\mathrm{f}} = 0 \quad \text{on } \Gamma, \tag{39}$$

which is done similarly to [35]. Thus, equations (37) and (39) together provide the boundary conditions imposed on chemical potential μ_* at the microscopic scale. The macroscopic scale, in turn, must provide μ_*^{M} and $\nabla_0^{\mathrm{M}}\mu_*^{\mathrm{M}}$ to enforce these boundary conditions.

The computational homogenisation for the mechanical part is well-established and can be found in textbooks, e.g. [31]. It does not change due to coupling with the diffusion-reaction. For completeness, it is useful to summarise the key points. The current position vector at the microscopic scale is represented as

$$\vec{x} = \vec{x}^{\mathrm{M}} + \boldsymbol{F}^{\mathrm{M}} \cdot \left(\vec{X} - \vec{X}^{\mathrm{ref}}\right) + \vec{x}^{\mathrm{f}}, \qquad \boldsymbol{F}^{\mathrm{M}} = \left(\nabla_0^{\mathrm{M}}\vec{x}^{\mathrm{M}}\right)^{\mathrm{T}}, \tag{40}$$

where $\boldsymbol{F}^{\mathrm{M}}$ and $\vec{x}^{\mathrm{M}}$ are the deformation gradient and the position vector at the macroscopic scale. It is easy to see that

$$\frac{1}{V_\Omega}\int_\Omega \boldsymbol{F}\,\mathrm{d}\Omega = \boldsymbol{F}^{\mathrm{M}} + \frac{1}{V_\Omega}\int_\Gamma \vec{x}^{\mathrm{f}}\vec{N}_\Gamma\,\mathrm{d}\Gamma. \tag{41}$$

An established way of forcing the last term of equation (41) to be zero is applying e.g. the prescribed displacement or the periodic boundary conditions (since this step is standard, the details are omitted). Since the mechanical equations are invariant with respect to the rigid-body motion, $\vec{x}^{\mathrm{M}}$ and $\vec{X}^{\mathrm{ref}}$ are not needed for the mechanical part. Thus, the macro scale must provide $\boldsymbol{F}^{\mathrm{M}}$ to enforce the boundary conditions at the micro scale.

2.4.2 Micro to macro transition

An established way of achieving the consistency between the micro and macro scales is the Hill-Mandel condition, which requires that the volume-averaged microscopic and the macroscopic internal energy rates are equal. The rate of change of the internal energy is the right-hand side of equation (7), which under assumptions of sections 2.3.1-2.3.2 becomes the following:

$$\frac{\mathrm{d}}{\mathrm{d}t}\left(\rho^0 u + \rho^0_* u_*\right) = -\frac{1}{M_*}\vec{j}\cdot\nabla_0\mu_* + \dot{c}\mu_* + \tilde{\boldsymbol{P}}^{\mathrm{T}} : \dot{\boldsymbol{F}} - \dot{\phi}\frac{\mu_*\zeta}{M_*}. \tag{42}$$

For convenience, the Hill-Mandel condition can be split into two parts — the diffusion-reaction and the mechanics parts:

$$I_{\mathrm{HM1}} = \frac{1}{V_\Omega}\int_\Omega \left(\mu_*\left(M_*\dot{c} - \zeta\dot{\phi}\right) - \vec{j}\cdot\nabla_0\mu_*\right)\mathrm{d}\Omega = \mu_*^{\mathrm{M}}\left(M_*\dot{c}^{\mathrm{M}} - \zeta\dot{\phi}^{\mathrm{M}}\right) - \vec{j}^{\mathrm{M}}\cdot\nabla_0\mu_*^{\mathrm{M}}, \tag{43}$$

$$I_{\mathrm{HM2}} = \frac{1}{V_\Omega}\int_\Omega \tilde{\boldsymbol{P}}^{\mathrm{T}} : \dot{\boldsymbol{F}}\,\mathrm{d}\Omega = \left(\tilde{\boldsymbol{P}}^{\mathrm{M}}\right)^{\mathrm{T}} : \dot{\boldsymbol{F}}^{\mathrm{M}}. \tag{44}$$

Using equation (5), it is easy to see that

$$\nabla_0\cdot\left(\mu_*\vec{j}\right) = \vec{j}\cdot\nabla_0\mu_* + \mu_*\nabla_0\cdot\vec{j} = \vec{j}\cdot\nabla_0\mu_* - \mu_*\left(M_*\dot{c} - \zeta\dot{\phi}\right). \tag{45}$$

Using equations (37) and (39), the left-hand side of equation (43) becomes

$$\begin{aligned} I_{\mathrm{HM1}} &= -\frac{1}{V_\Omega}\int_\Gamma \vec{N}_\Gamma\cdot\vec{j}\mu_*\,\mathrm{d}\Gamma = -\frac{1}{V_\Omega}\int_\Gamma \vec{N}_\Gamma\cdot\vec{j}\left(\mu_*^{\mathrm{M}} + \nabla_0^{\mathrm{M}}\mu_*^{\mathrm{M}}\cdot\left(\vec{X} - \vec{X}^{\mathrm{ref}}\right)\right)\mathrm{d}\Gamma = \\ &= -\mu_*^{\mathrm{M}}\frac{1}{V_\Omega}\int_\Omega \nabla_0\cdot\vec{j}\,\mathrm{d}\Omega - \nabla_0^{\mathrm{M}}\mu_*^{\mathrm{M}}\cdot\frac{1}{V_\Omega}\int_\Gamma\left(\vec{X} - \vec{X}^{\mathrm{ref}}\right)\vec{N}_\Gamma\cdot\vec{j}\,\mathrm{d}\Gamma. \end{aligned} \tag{46}$$

Using equation (5) again and equating the right-hand sides of equations (46) and (43) results in

$$\dot{c}^{\mathrm{M}} = \frac{1}{V_\Omega}\int_\Omega \dot{c}\,\mathrm{d}\Omega \tag{47}$$

$$\dot{\phi}^{\mathrm{M}} = \frac{1}{V_\Omega}\int_\Omega \dot{\phi}\,\mathrm{d}\Omega \tag{48}$$

$$\vec{j}^{\mathrm{M}} = \frac{1}{V_\Omega}\int_\Gamma \left(\vec{X} - \vec{X}^{\mathrm{ref}}\right)\vec{N}_\Gamma\cdot\vec{j}\,\mathrm{d}\Gamma. \tag{49}$$

Relations (47) and (49) have been obtained in the past by multiple authors, in particular [37]. Thus, at the macroscopic scale, equation (35), the reaction and the concentration change rates ($\dot{c}^{\mathrm{M}}$ and $\dot{\phi}^{\mathrm{M}}$, respectively) are not calculated from other macroscopic quantities, but are obtained from the microscopic scale by volume-averaging, as well as diffusive flux $\vec{j}^{\mathrm{M}}$. At the macroscopic scale, the unknown variable is field μ_*^{M}, with respect to which equation (35) must be solved.

The mechanics part is again standard. Using equations (36) and (40), as well as the appropriate boundary conditions, e.g. periodic, it is easy to show that equation (44) is fulfilled if

$$\tilde{\boldsymbol{P}}^{\mathrm{M}} = \frac{1}{V_\Omega}\int_\Omega \tilde{\boldsymbol{P}}\,\mathrm{d}\Omega. \tag{50}$$

Thus, at the macroscopic scale, equation (36) is solved with respect to the macroscopic displacement, while the macroscopic Piola-Kirchhoff stress is obtained from the microscopic scale by volume-averaging. The quantities that are passed between the macro and the micro scales are summarised in figure 1.

2.5 Computational scheme

The full mechanics-diffusion-reaction-temperature problem comprises of equations (5), (6), (23), (24), which must be solved with respect to c, ϕ, T, $\vec{u}$ that are the functions of t and $\vec{X}$, and which contain quantities that are defined by equations (8), (15)-(17), (19)-(21); additionally, functional dependencies for $\vec{b}$, $\vec{b}_*$, R, p_*, ω, f, $\boldsymbol{F}_{\mathrm{C}}$ must be specified for the particular problem.

The simplified mechanics-diffusion-reaction problem under assumptions of sections 2.3.1-2.3.2 and for isothermal conditions comprises of equations (5), (23), (31), which must be solved with respect to c, ϕ, $\vec{u}$ that are the functions of t and $\vec{X}$, and which contain quantities that are defined by equations (15), (17), (21), (32), (34); additionally, functional dependencies for ω, f, $\boldsymbol{F}_{\mathrm{C}}$ must be specified for the particular problem.

The two-scale mechanics-diffusion-reaction problem comprises of equations (35), (36) at the macroscopic scale, which must be solved with respect to μ_*^{M}, $\vec{u}^{\mathrm{M}}$ that the functions of t and $\vec{X}^{\mathrm{M}}$. At each macroscopic point, macroscopic quantities are defined as averages of the microscopic quantities according to equations (47)-(50). Within each microscopic domain, the simplified mechanics-diffusion-reaction problem is solved with the corresponding boundary conditions, which depend on μ_*^{M}, $\nabla_0^{\mathrm{M}}\mu_*^{\mathrm{M}}$, $\boldsymbol{F}^{\mathrm{M}}$ at each corresponding macroscopic point.

2.5.1 Local problem

As mentioned above, the local problem comprises of equations (5), (23), (31). The underlying equations of the problem can be solved using the finite-element method, requiring the weak forms of the equations that can be obtained in the standard way. However, a care must be taken when representing the time derivatives in the discrete form. The use of the implicit time-stepping in all equations will lead to a fully-coupled system of equations, which must be solved using the Newton-Raphson method in general case.

From the implementational point of view, it is more convenient to solve the equations sequentially within one time step. To facilitate this, the explicit time-stepping to handle the reaction can be used. It is easy to see that the resulting weak problem formulation consists in finding c_n, ϕ_n, $\vec{u}_n$, such that

$$\int_{\Omega}\left(M_*\frac{c_n - c_{n-1}}{\Delta t}\theta - \vec{j}_n\cdot\nabla_0\theta - \zeta\omega_{n-1}\theta\right)\mathrm{d}\Omega + \int_{\Gamma}\vec{N}_{\Gamma}\cdot\vec{j}_n\theta\,\mathrm{d}\Gamma = 0, \tag{51}$$

$$\int_{\Omega}\tilde{\boldsymbol{P}}_n : \nabla_0\vec{\theta}\,\mathrm{d}\Omega - \int_{\Gamma}\tilde{\boldsymbol{P}}_n : \vec{N}_{\Gamma}\vec{\theta}\,\mathrm{d}\Gamma = 0, \tag{52}$$

$$\frac{\phi_n - \phi_{n-1}}{\Delta t} = \omega_{n-1}, \tag{53}$$

for any test functions θ, $\vec{\theta}$, where the unknown and the test functions belong to the appropriate functional spaces. Here, subscripts n and $n-1$ indicate that the quantities are taken at the corresponding time steps.

Diffusive flux $\vec{j}$ depends on $\nabla_0\mu_*$, which depends on derivatives of $\vec{u}$ (via $\boldsymbol{P}$ and $\boldsymbol{F}$) in general case. However, in mechanics-diffusion-reaction problems, a solid skeleton approach is sometimes adopted, e.g. [26], which implies that the non-mechanical deformation does not depend on concentration c and depends only on reaction extent ϕ, i.e. $\partial\boldsymbol{F}_{\mathrm{C}}/\partial c = \boldsymbol{0}$. In this case, equations (51) and (52) can be solved sequentially within one time step, as equation (51) does not depend on $\vec{u}_n$ (but still depends on $\vec{u}_{n-1}$ via ω_{n-1}). Thus, within one step, equation (53) is solved first with respect to ϕ_n, then equation (51) is solved to find c_n, and finally equation (52) is solved with respect to $\vec{u}_n$.

If the solid-skeleton approach is not adopted, then $\vec{j}_n$ in equation (51) can be taken to be dependent on derivatives of c_n and $\vec{u}_{n-1}$. Such hybrid explicit-implicit scheme will still allow solving equations (51) and (52) separately, without the need to form one big system of equations.

The suggested-above numerical approach aims at illustrating schematically the handling of the time derivatives in the equations. As for the spatial derivatives, more complex finite-element approaches can be used, e.g. XFEM [42–44] or CutFEM [45, 46] for handling cracks/interfaces. In this case, the weak forms will have additional terms, depending on the approach.

2.5.2 Two-scale problem

First, the weak problem formulation of the macroscopic problem is written that consists in finding μ^{M}_{*n}, $\vec{u}^{\mathrm{M}}_n$, such that

$$\int_{\Omega^{\mathrm{M}}} \left(M_* \dot{c}^{\mathrm{M}}_n \theta^{\mathrm{M}} - \vec{j}^{\mathrm{M}}_n \cdot \nabla^{\mathrm{M}}_0 \theta^{\mathrm{M}} - \zeta \dot{\phi}^{\mathrm{M}}_n \theta^{\mathrm{M}} \right) \mathrm{d}\Omega^{\mathrm{M}} + \int_{\Gamma^{\mathrm{M}}} \vec{N}^{\mathrm{M}}_{\Gamma} \cdot \vec{j}^{\mathrm{M}}_n \theta^{\mathrm{M}} \, \mathrm{d}\Gamma^{\mathrm{M}} = 0, \tag{54}$$

$$\int_{\Omega^{\mathrm{M}}} \tilde{\boldsymbol{P}}^{\mathrm{M}}_n : \nabla^{\mathrm{M}}_0 \vec{\theta}^{\mathrm{M}} \, \mathrm{d}\Omega^{\mathrm{M}} - \int_{\Gamma^{\mathrm{M}}} \tilde{\boldsymbol{P}}^{\mathrm{M}}_n : \vec{N}^{\mathrm{M}}_{\Gamma} \vec{\theta}^{\mathrm{M}} \, \mathrm{d}\Gamma^{\mathrm{M}} = 0, \tag{55}$$

for any test functions θ^{M}, $\vec{\theta}^{\mathrm{M}}$, where the unknown and the test functions belong to the appropriate functional spaces. Subscript n indicate that the quantities are taken at the current time step. The macroscopic domain, its boundary and the external normal to the boundary are denoted as Ω^{M}, Γ^{M} and $\vec{N}^{\mathrm{M}}_{\Gamma}$, respectively.

It must be emphasised that at each material point (integration point), $\dot{c}^{\mathrm{M}}_n$, $\dot{\phi}^{\mathrm{M}}_n$, $\vec{j}^{\mathrm{M}}_n$, $\tilde{\boldsymbol{P}}^{\mathrm{M}}_n$ are obtained by volume-averaging of the quantities of the corresponding RVE using equations (47)-(50). Since the problem is non-linear, a global Newton-Raphson (NR) loop should be employed to find the macroscopic unknowns, while each local problem should have a local NR loop to find the microscopic quantities.

The local problem is solved with respect to concentration c, however, the boundary conditions are applied in the form of chemical potential μ_* according to equations (37) and (39). Depending on the expression for the chemical potential, this might create difficulties for convergence of the global NR loop. In particular, during the development of the code, it has been found that when the ideal gas chemical potential is used, $\mu_* = \mu_0 + R_{\mathrm{g}} T \ln \left(c/c_0 \right)$, the exponential dependency between c and μ_* leads to NR convergence problems when c is close to zero.

A possible solution for such NR convergence problems consists in two parts. The first part is to introduce a different macroscopic degree of freedom $\tilde{c}^{\mathrm{M}} = c_0 \exp \left(\left(\mu^{\mathrm{M}}_* - \mu_0 \right) / R_{\mathrm{g}} T \right)$ and solve the macroscopic problem with respect to $\tilde{c}^{\mathrm{M}}$ and not μ^{M}_*. It should be noted that $\tilde{c}^{\mathrm{M}}$ is not equal to c^{M}, as the latter is obtained from the RVE by volume-averaging. Furthermore, $\tilde{c}^{\mathrm{M}}$ and c^{M} are defined at different points — the former is defined at the nodes (as DOFs), while the latter is defined at the integration points (since RVEs are associated with the integration points). The second part is linearising the boundary conditions for the RVE with respect to $\tilde{c}^{\mathrm{M}}$ and $\nabla^{\mathrm{M}}_0 \tilde{c}^{\mathrm{M}}$.

3 Numerical examples

The proposed framework has been implemented in Matlab. The main feature of the implementation is the use of the CutFEM method [46, 47] to handle the local problem. The CutFEM method originates from [45, 48] and has been recently extended to large-deformation problems of solid mechanics [40, 49]. This allows creating RVEs with interfaces, e.g. inclusion-matrix, and handling these interfaces in a computationally-efficient way by creating a structured background mesh and allowing the interfaces to cut through the elements. The computational handling of the mechanical problem has already been described in [49]; therefore, only the diffusion-reaction part is covered in appendix A.

3.1 Link to experimental studies

The numerical examples below illustrate the elements of the proposed theory, and are inspired by experimental observations for Si-based Li-ion battery systems. In particular, the first computational example is related to [50], where it has been experimentally observed that the chemical reaction between Si and Li in coated Si nanoparticles locks due to the mechanical stresses. The third computational example follows [51, 52], where it has been found that various irreversible mechanical degradation processes occur at the electrode microscale, which includes active particles (where the reaction takes place) detaching from the surrounding matrix material, and leading to the capacity fade. Further discussion on the outcome of numerical simulations in relation to experimental results is provided in the subsequent sections below (3.4 and 3.6).

3.2 Constitutive relations

As mentioned above, a particular problem must be supplemented by the constitutive relations. The laws assumed for the numerical examples are relatively simple, but are sufficient to demonstrate the physical effects in the coupled mechanics-diffusion-reaction problem. The non-mechanical deformation is assumed to depend only on the reaction extent and is assumed to be flat:

$$\boldsymbol{F}_{\mathrm{C}} = (1 + g\phi)\,(\vec{e}_1\vec{e}_1 + \vec{e}_2\vec{e}_2) + \vec{e}_3\vec{e}_3, \tag{56}$$

where parameter g controls the amount of material deformation due to the reaction. The free energy density is assumed to consist of three parts corresponding to the mechanics, the diffusion and the reaction:

$$\begin{aligned} f = f_0 + J_{\mathrm{C}} K\,(J_{\mathrm{E}} - 1 - \ln J_{\mathrm{E}}) + J_{\mathrm{C}}\frac{G}{2}\left(J_{\mathrm{E}}^{-2/3}\boldsymbol{F}_{\mathrm{E}} : \boldsymbol{F}_{\mathrm{E}}^{\mathrm{T}} - 3\right) + \\ + R_{\mathrm{g}}T\left(c \ln\frac{c}{c_0} - c\right) + R_{\mathrm{g}}T\frac{\rho^0 n_{\mathrm{t}}}{M_{\mathrm{u}} n_{\mathrm{u}}}\,(\phi\ln\phi - \phi)\,, \end{aligned} \tag{57}$$

where f_0 is a constant, $J_{\mathrm{C,E}} = \det \boldsymbol{F}_{\mathrm{C,E}}$, parameters K and G are the bulk and shear moduli, R_{g} is the universal gas constant, c_0 is some reference concentration, n_{t} and n_{u} are the stoichiometric coefficients of the reaction corresponding to the transformed and the untransformed solid, respectively, M_{u} is the molar mass of the chemically untransformed solid. The proportionality tensor between the gradient of the chemical potential and the diffusive flux is assumed to be

$$\boldsymbol{K} = Dc\boldsymbol{I}, \tag{58}$$

where D is the diffusivity parameter and $\boldsymbol{I}$ is the identity tensor. Finally, the reaction rate dependence on the chemical affinity is assumed to be similar to one proposed in [16]:

$$\omega = k_*\left(1 - \exp\left(-\frac{M_{\mathrm{u}}A}{\rho^0 R_{\mathrm{g}}T}\right)\right)\left(\frac{c}{c_0}\right)^{n_*/n_{\mathrm{u}}}, \tag{59}$$

where k_* is the kinetic constant, n_* is the stoichiometric coefficient of the reaction corresponding to the gas.

As seen from equation (57), for the numerical simulations, the pressure of the gas is neglected. Since the purpose of the numerical examples is to provide the simplest possible demonstration of the capabilities of the proposed theory and the two-scale modelling scheme, absence of p_* is assumed to avoid formulating the constitutive equations for it. This is also a valid assumption in a number of cases, for example, when the reaction between Li and Si is considered, since the reaction-induced volumetric swelling [4] of up to 300% produces stresses that should be far greater than pressure of the diffusing Li ions.

For the numerical examples, the elastic moduli of the solid are assumed to be independent of the reaction extent. In case when real materials are modelled quantitatively, this dependency is not difficult to include. Parameters K and G simply become some functions of reaction extent ϕ. In this case, the experimental information on the dependence of the elastic moduli on the reaction extent is required.

3.2.1 On mechanics-diffusion-reaction coupling

In the theoretical framework, presented in section 2, all three processes are of course fully coupled. In particular, equation (11) shows that, in general, both c and ϕ can produce transformation strain, which (in most cases) will lead to the emergence of the mechanical stresses. Equation (17) shows that μ_* depends on $\tilde{\boldsymbol{P}}$, and since $\vec{j}$ depends on $\nabla_0\mu_*$ via $\vec{q}$, the mechanical stresses influence the diffusion process. Equation (19) shows that A depends on $\tilde{\boldsymbol{P}}$, and since A is the driving force for the reaction according to equation (23), the mechanical stresses influence the reaction kinetics. The interdependence between the diffusion and the reaction processes obviously follows from equations (5), (19) and (23).

When equations (17) and (19) are inspected closely, it can be seen that $\tilde{\boldsymbol{P}}$ is multiplied by $\partial\boldsymbol{F}_{\mathrm{C}}/\partial c$ and $\partial\boldsymbol{F}_{\mathrm{C}}/\partial\phi$, respectively. Therefore, the diffusion process depends directly on the stresses if $\boldsymbol{F}_{\mathrm{C}}$ depends on c, while the reaction process depends directly on the stresses if $\boldsymbol{F}_{\mathrm{C}}$ depends on ϕ.

In the constitutive equations used for the numerical examples, equation (56), it is assumed that $\boldsymbol{F}_{\mathrm{C}}$ depends only on ϕ. This is so-called solid skeleton approach and it has been used historically by other researchers, e.g. [26].

In addition, it should be emphasised that in the above, only the direct influence of the mechanical stresses on the diffusion process is discussed. Since mass balance equation (5) contains the source/sink term, which is proportional to the chemical reaction rate, the mechanics-reaction coupling leads to the indirect influence of the mechanical stresses on the diffusion process.

3.2.2 Inclusion-matrix interface

In section 3.6, an RVE with the microstructure is considered, in which an inclusion is embedded into a matrix. The problem assumes that the inclusion-matrix interface allows debonding. The entire computational domain Ω is split into subdomains $\Omega_{\pm}$ by interface Γ_{*}. The following the interface conditions are used for the linear momentum balance equation:

$$\boldsymbol{P}_{+} \cdot \vec{N}_{\mathrm{I}} = \boldsymbol{P}_{-} \cdot \vec{N}_{\mathrm{I}}, \tag{60}$$

$$\left(\boldsymbol{P}_{+} + \boldsymbol{P}_{-}\right) \cdot \vec{N}_{\mathrm{I}} = -2\chi \left(\vec{u}_{+} - \vec{u}_{-}\right) \exp\left(-\delta \left|\vec{u}_{+} - \vec{u}_{-}\right|\right), \tag{61}$$

where $\vec{N}_{\mathrm{I}}$ is the interface normal, defined as the outer normal to Ω_{+}, subscripts '+' and '−' indicate quantities belonging to different sides of the interface, χ and δ are the interface parameters. Equation (60) is the continuity of tractions at the interface (i.e. there are no additional forces acting at the interface). Equation (61) is the so-called exponential cohesive zone law, derived from the energy of the interface that can describe a wide variety of fracture behaviours [53]. The minus sign of the right-hand side of equation (61) is due to the orientation of $\vec{N}_{\mathrm{I}}$.

To account for the influence of the interface opening on the diffusion, the following interface conditions are used for the mass balance equation:

$$\vec{j}_{+} \cdot \vec{N}_{\mathrm{I}} = \vec{j}_{-} \cdot \vec{N}_{\mathrm{I}}, \tag{62}$$

$$\tilde{\kappa} \left(\vec{j}_{+} + \vec{j}_{-}\right) \cdot \vec{N}_{\mathrm{I}} = 2\left(c_{+} - c_{-}\right), \qquad \tilde{\kappa} = \kappa \left|\vec{u}_{+} - \vec{u}_{-}\right|^{2}, \tag{63}$$

where κ is the interface parameter. Equations (62) and (63) have the structure of membrane boundary conditions [54], where $\tilde{\kappa}$ is the inverse of the membrane permeability coefficient. It is assumed that when interface separation takes place, it creates a barrier for the diffusion, similar to what a membrane would create. Intuitively, one might think that the permeability of such barrier should drop rapidly with the interface opening; therefore, the dependence of $\tilde{\kappa}$ on $|\vec{u}_{+} - \vec{u}_{-}|$ is introduced in an ad hoc way. The plus sign of the right-hand side of equation (63) is again due to the orientation of $\vec{N}_{\mathrm{I}}$.

3.3 Stationary homogeneous solution, reaction locking

There is a number of physical effects arising in the coupled mechanics-diffusion-reaction problem, one of which is the chemical reaction locking due to mechanical stresses. Within the continuum mechanics field, this effect has been first modelled in [26, 55–58] for the stress-affected localised chemical reactions (taking place at a propagating interface between the chemically transformed and untransformed phases), where analytical and numerical studies were performed based on the concept of the chemical affinity tensor. In the case of localised reactions, the chemical affinity is a tensorial quantity due to the chemical reaction taking place at an oriented surface element, as opposed to the scalar chemical affinity, equation (19), that arises when the chemical reaction takes place in an elementary volume element.

The easiest way to understand this effect is to consider mechanically constrained homogeneous material, i.e. $\boldsymbol{F} = \boldsymbol{I}$. From equation (23), it can be seen that the chemical reaction stops when $\omega = 0$. The diffusion, in turn, continues until the concentration field is at the saturation level, i.e. $c = c_0$. Substituting these conditions as well as the constitutive relations into $\omega = 0$ gives

$$\begin{aligned} 1 - \phi_{\mathrm{L}}^{n_{\mathrm{t}}/n_{\mathrm{u}}} \exp\Bigg(\frac{M_{\mathrm{u}}}{\rho^{0} R_{\mathrm{g}} T} g\left(1 + g\phi_{\mathrm{L}}\right) \Bigg(4K \ln\left(1 + g\phi_{\mathrm{L}}\right) + \\ + \frac{G}{3}\left(4\left(1 + g\phi_{\mathrm{L}}\right)^{-2/3} + 5\left(1 + g\phi_{\mathrm{L}}\right)^{4/3} - 9\right)\Bigg)\Bigg) = 0, \end{aligned} \tag{64}$$

where ϕ_{L} is the value of the reaction extent at which the reaction locks. When equation (64) is solved numerically with respect to ϕ_{L}, it can be seen that for non-zero g, the value of ϕ_{L} is less than 1, i.e. the expansion due to the reaction creates mechanical stresses, which affect the reaction rate such that the full transformation of the material cannot be achieved — the reaction stops earlier. The reaction extent at locking will of course be dependent on parameters g, K, G and $M_{\mathrm{u}} \left(\rho^{0} R_{\mathrm{g}} T\right)^{-1}$.

3.4 Computational example — reaction locking

This section aims at verifying the implementation of the coupling. First, the reaction locking effect is modelled computationally and is then compared to the analytical solution from equation (64). Afterwards,

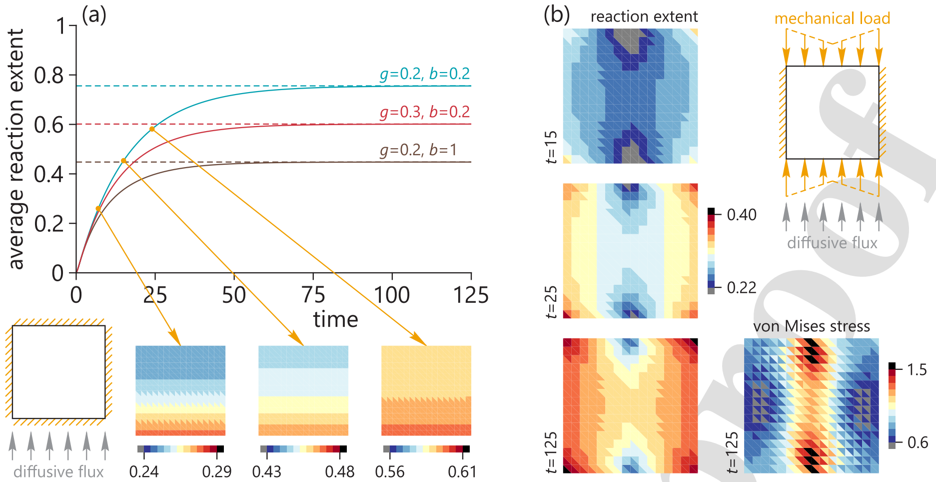

Figure 2: The time evolution of the volume-average reaction extent compared to the analytical stationary solution (a) and spatial distribution of the reaction extent (insets) for the mechanically constrained problem. For brevity, M_u/ρ^0 is denoted as b. Snapshots of the spatial distribution of the reaction extent and the von Mises stress (b) for the mechanical problem with the indented boundaries. Reference configuration of the geometry is used for the contour plots.

a non-homogeneous stress distribution is created, leading to a non-homogeneous reaction extent at the locked state.

Since the purpose of the present paper is the presentation of the computational framework, units are omitted for all quantities. The unit square geometry is considered. The geometry is meshed using linear triangular finite elements composing a structured mesh. All elements of the mesh are isosceles right triangles with side lengths of Δx. In the mechanical part of the problem, the plane strain case is considered.

The values of parameters M_*, $R_\mathrm{g}T$, c_0, D, k_*, n_t, n_u, n_* are taken to be equal to 1. The reaction parameter is taken to be $\zeta = -1$, indicating the consumption of the diffusive species due to the reaction. The elastic parameters are taken to be $K = 10$ and $G = 2$. Parameter g is varied — values of 0.2 and 0.3 are used to demonstrate different cases. Parameter M_u/ρ^0 is also varied — values of 0.2 and 1 are used. Numerical parameters $\Delta x = 1/16$ and $\Delta t = 1/4$ are used.

The first problem considers a fully constrained domain; therefore, $\vec{u} = \vec{0}$ is applied at the external boundary of the domain. The second problem creates a non-homogeneous stress state; therefore, $\vec{u} = \vec{0}$ is enforced at the left and the right boundaries and

$$u_1 = 0, \qquad u_2 = \vec{N}_\Gamma \cdot \vec{e}_2 \left(0.2\,|X_1 - 0.5| - 0.1\right)$$

is applied at the top and the bottom boundaries. For the diffusion problem,

$$\vec{N}_\Gamma \cdot \vec{j} - \alpha\,(c - c_\mathrm{b}) = 0$$

is applied at the bottom boundary, with $\alpha = 0.1$ and $c_\mathrm{b} = 1$, and $\vec{N}_\Gamma \cdot \vec{j} = 0$ is applied at the other boundaries, where c_b is some reference concentration having the physical meaning of the maximum achievable concentration. Furthermore, $c = 0$ and $\phi = 0$ are used for the initial conditions.

Both problems are illustrated in figure 2. For the first problem, the volume-average reaction extent is calculated (similarly to equation (48)), plotted as a function of time (solid line) and compared to the analytical solution (dashed line, ϕ_L obtained from equation (64)). It can be seen that as time increases, the computational solution approaches the analytical solution for different parameter combinations. Within the transient regime, the reaction extent gradually increases from the bottom to the top of the domain, which is of course due to the supply of the diffusive species from the bottom boundary.

For the second problem, the spatial distributions of the reaction extent and the von Mises stress[1] are plotted for different moments of time. For this problem, $g = 0.2$ and $M_\mathrm{u}/\rho^0 = 1$ are used. Since the parameters are the same as for the first problem, it can be expected that at $t = 125$ the stationary solution is already reached. It can be seen that the reaction extent at the locked state is inhomogeneous with lower values corresponding to zones of high stresses.

The chemical reaction locking due to the mechanical stresses is an experimentally-observed effect. For example, in [50], it has been observed for the reaction between Si and Li in coated Si nanoparticles. Different types of coatings led to different completion degrees of the reaction before locking. Coatings, which constrain the material more, lead to higher stresses, resulting in the smaller lithiation degree (i.e. earlier reaction locking). Here, this effect is modelled in a somewhat different setting, for a fully-constrained plane strain geometry. However, the trend is qualitatively similar — higher volumetric expansion due to the reaction (parameter g) leads to higher stresses and hence to the reaction locking at an earlier completion degree.

3.5 Computational example — two-scale simulation, perfect inclusion-matrix interface

This section aims at demonstrating the implementation of the two-scale framework. The plane-strain 2D problem is considered. A composite material with a microstructure is modelled. The microstructure represents circular inclusions embedded into a matrix and arranged in a regular square grid. The chemical reaction can take place only within the inclusions, while the diffusion can take place both in the matrix and in the inclusions. The composite material with the initially chemically-untransformed inclusions is first subjected to the influx of the diffusive species, leading to the chemical reaction within the inclusions, and then subjected to the boundary conditions creating the outflow of the diffusive species, leading to the reverse chemical reaction. Such example can roughly correspond to an energy-storage heterogeneous material undergoing one charge/discharge cycle.

The two-scale representation is used to model the composite material, with the homogeneous macroscopic scale and the RVEs with inclusions at the microscopic scale. The material is constrained at the macroscopic scale; therefore, this scale is assumed to be uniform mechanically and $\boldsymbol{F}^\mathrm{M} = \boldsymbol{I}$ is prescribed, without solving the macroscopic linear momentum balance equation.

The influx/outflow takes place only at the left boundary of the rectangular macroscopic geometry of the composite material. This boundary condition is also assumed to be uniform along the boundary; therefore, the macroscopic diffusion and reaction extent fields are non-uniform only in the horizontal dimension. Thus, for the macroscopic diffusion-reaction equation, a 1D domain of length 10 is taken with macroscopic spatial step $\Delta x = 2.5$ and the following boundary conditions:

$$\vec{e}_1 \cdot \vec{j}^\mathrm{M} + \alpha\left(\tilde{c}^\mathrm{M} - c_\mathrm{b}\right) = 0, \qquad \text{at the left boundary,}$$
$$\vec{e}_1 \cdot \vec{j}^\mathrm{M} = 0, \qquad \text{at the right boundary,}$$

where $\alpha = 0.1$. Here, $c_\mathrm{b} = 1$ for $t < 250$, creating influx of the diffusive species, and $c_\mathrm{b} = 0$ for $t \geq 250$, creating the outflow of the diffusive species leading to a reverse reaction.

For the RVE, the same as in the previous example unit square geometry is used, with the same mesh; however, now there is a circular interface with the radius of 0.27 separating the inclusion (inner subdomain with $K = 10$ and $G = 2$, where the reaction takes place, $k_* = 1$) and the matrix (outer subdomain with $K = 20$ and $G = 4$, where there is no chemical reaction, $k_* = 0$). The CutFEM method handles the interface intersecting the elements. Perfect interface conditions are used, i.e. equations (60) and (62) as well as $\vec{u}_+ = \vec{u}_-$ and $c_+ = c_-$. The periodic boundary conditions are prescribed for the mechanical part. For the diffusion problem, $c = 0$ and $\phi = 0$ are used for the initial conditions. The remaining parameters are the same as in the second problem of section 3.4.

The evolution of macroscopic concentration $\tilde{c}^\mathrm{M}$ is illustrated in figure 3. The profile is decaying is space, since the supply of the diffusive species is at the left boundary, and the concentration grows in time up to $t = 250$. From this moment onwards, the concentration decreases. Within the RVEs, the reaction extent is close to being uniform inside the inclusion, with small variations. During the first stage, when RVEs are compared, the reaction extent decreases from left to right. Higher reaction extent of course corresponds to higher expansion of the material, leading to higher stresses.

[1] This stress is defined as usual as $\sigma_\mathrm{VM} = \sqrt{(3/2)\,\boldsymbol{\sigma}^\mathrm{d} : \boldsymbol{\sigma}^\mathrm{d}}$, where $\boldsymbol{\sigma}^\mathrm{d} = \boldsymbol{\sigma} - (1/3)\,\boldsymbol{\sigma} : \boldsymbol{II}$ and $\boldsymbol{\sigma} = J^{-1}\boldsymbol{P} \cdot \boldsymbol{F}^\mathrm{T}$.

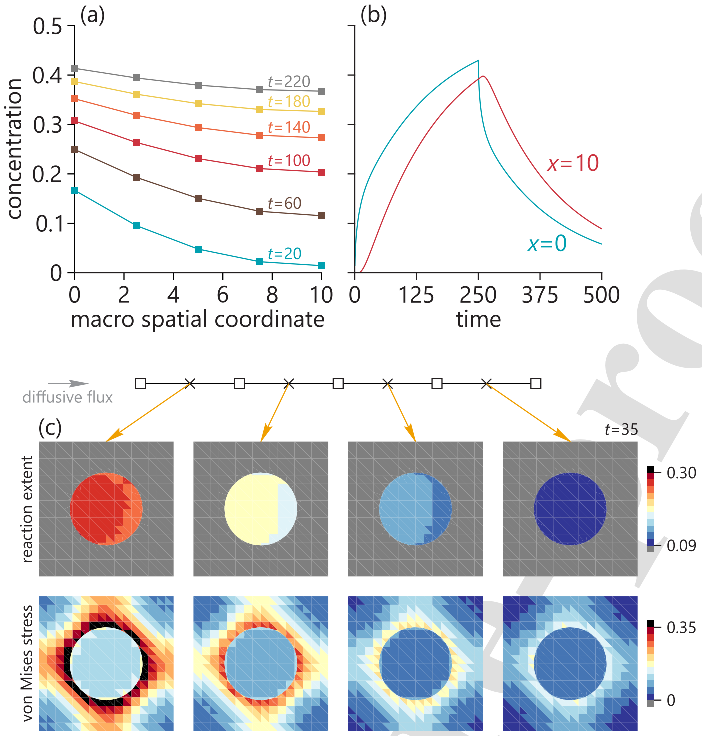

Figure 3: The time evolution of the spatial distribution of the concentration at the macroscopic scale in the two-scale simulation (a) and the dependence of the concentration at the left and the right edges of the macroscopic domain on time (b). The schematic illustration of the macroscopic 1D domain (centre) and snapshots of the spatial distribution of the reaction extent and the von Mises stress in the RVEs (c). Reference configuration of the geometry is used for the contour plots.

3.6 Computational example — two-scale simulation, imperfect inclusion-matrix interface

This section aims at demonstrating a capability to model more complex physical effects in the microstructure, in particular, debonding at the inclusion-matrix interface and the influence of the interface damage on the diffusion and the reaction.

The problem setup is the same as in the previous example, apart from few differences. The inclusions are initially chemically transformed and the concentration is at the saturation level. The boundary conditions create the outflow of the diffusive species from the domain, leading to the reverse reaction. The decrease of the reaction extent leads to shrinkage of the inclusions and consequently to the interface damage. Two different scenarios are considered, corresponding to the perfectly transparent interface for the diffusion and to the interface permeability influenced by the interface damage.

The same macroscopic boundary conditions are used, with $c_\mathrm{b} = 0$. The interface conditions (60)-(63) are used with $\chi = 10$ and $\delta = 10$. Two different scenarios are considered $\kappa = 0$ and $\kappa = 10^7$. For the diffusion problem, $c = 1$ and $\phi = 1$ are used for the initial conditions. The chemical deformation gradient is changed to

$$\boldsymbol{F}_\mathrm{C} = (1 + g(\phi - 1))(\vec{e}_1\vec{e}_1 + \vec{e}_2\vec{e}_2) + \vec{e}_3\vec{e}_3, \tag{65}$$

indicating that $\boldsymbol{F}_\mathrm{C} = \boldsymbol{I}$ initially.

The evolution of volume-average reaction extent within the inclusions and snapshots of the RVE geometry (corresponding to the first element of the macroscopic domain) is shown in figure 4. The reverse reaction takes place — the reaction extent decreases in time. Furthermore, the reaction extent in

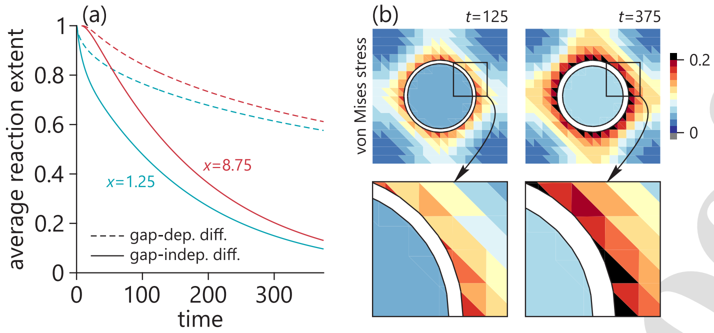

Figure 4: The time-dependence of the volume-average reaction extent within the inclusions in the RVEs corresponding to the first and the fourth elements of the macroscopic domain (a). Snapshots of the spatial distribution of the von Mises stress in the RVEs in the current configuration of the geometry also showing debonding at the interface for the case of gap-independent interface permeability (b).

the left element of the macroscopic geometry decays faster than in the right element, due to the outflow of the diffusive species from the left. The rate of decay is influenced by the interface conditions — when the interface permeability depends on the interface damage, the rate of the outflow of the diffusive species from the inclusion is significantly decreased, leading to a slower reverse reaction rate inside the inclusion.

The influence of the interface damage on the diffusion and the reaction processes is observed experimentally. For example, in [51], graphite-silicon composite electrode materials of Li-ion batteries have been cycled and it has been experimentally observed that active Si particles (where the reaction takes place) can detach from the carbon-binder matrix material, leading to the capacity fade. The formation of gaps between the active particles and the matrix prevents Li ions from diffusing into and out of the active material and participating in the chemical reaction. Here, this effect is modelled in a somewhat different setting. Since no mechanical irreversibility (e.g. material plasticity or damage) is built into the constitutive relations presented in section 3.2, the formation of the gap and its influence on the diffusion and the reaction processes is investigated within one 'cycle', but with various inclusion-matrix interface parameters. Qualitatively similar trend can be seen — when it is assumed that the gap reduces the permeability of the inclusion-matrix interface, the reaction rate inside the inclusions is inhibited due to inability of the diffusive species to be transported out of the inclusions.

4 Conclusions

A general thermo-chemo-mechanical theory and the corresponding two-scale framework was proposed in the present paper to model chemo-mechanical processes in advanced heterogeneous materials. The theory was derived for thermo-chemo-mechanical case under reversible (non-linear elastic) finite strains, with an explanation of how its future extensions to irreversible (inelastic) mechanical deformations can be incorporated into the theoretical framework. As the kinetics of the transport and the reaction processes in the framework are described as separate, they can be affected by mechanical stresses in different ways. For the purpose of incorporating into a two-scale approach using computational homogenisation, the framework was simplified to the the quasi-static case. A detailed computational scheme to handle the equations was presented. For numerical examples, a set of simple constitutive laws was assumed, and the framework was implemented in Matlab for a 2D-micro-to-1D-macro two-scale approach, using the CutFEM method that handles the evolution of interfaces in a computationally-efficient way. Several numerical examples were included in the paper to show ultimately the effect of reaction locking by mechanical stresses and a more complex scenario when the diffusive species propagate through the microstructure with inclusions undergoing both a chemical reaction and the interfacial damage (debonding from the matrix) due to chemically-induced contraction. The proposed approach can be used to asses the effects of chemical stresses on chemo-physical processes occurring in advanced systems such as batteries, and exploit a more efficient material use at the micro scale, given the macroscopically applied operating conditions.

Acknowledgements

The authors acknowledge the financial support from the EU Horizon 2020 project ECO2LIB, number 875514. The authors are extremely grateful for the invaluable feedback and numerous suggestions provided by two anonymous reviewers that substantially improved the paper.

Appendix A Computational handling of diffusion-reaction using CutFEM

Weak forms (51) and (52) are the simplest (standard FEM) weak forms of the corresponding equations. They illustrate the handling of the time derivatives in the equations. However, one of the main features of the current work is consideration of the microstructures with interfaces and handling them using computationally-efficient non-conforming-mesh method, more specifically, CutFEM. The mechanical part and the finite-element formulation is covered in the previous publication by the authors [49]; furthermore, this appendix relies on the reader being familiar with the basis of the CutFEM method, explained in e.g. [47, 59, 60]. To complete the description of the computational part, this appendix summarises the diffusion-reaction problem with interfaces and its weak form used in CutFEM.

The strong form of the problem consists in equation (5) with some boundary conditions and with interface conditions (62) and (63). For brevity, the latter interface condition is rewritten as:

$$\tilde{\kappa} p = [\![c]\!], \qquad p = \left\langle \vec{j} \right\rangle \cdot \vec{N}_\mathrm{I}. \tag{66}$$

First, the energy of the interface is written as

$$\mathit{\Pi}_* = \int_{\mathit{\Gamma}_*} \left(\frac{1}{2} S_h \left([\![c]\!] - \tilde{\kappa} p \right)^2 + p\, [\![c]\!] - \frac{1}{2} \tilde{\kappa} p^2 \right) \mathrm{d}\mathit{\Gamma}_*, \qquad S_h = \left(\frac{h}{\lambda} + \tilde{\kappa} \right)^{-1}, \tag{67}$$

where h is the typical mesh size and λ is the penalty parameter. The variation of $\mathit{\Pi}_*$ results in

$$\delta \mathit{\Pi}_* = \int_{\mathit{\Gamma}_*} \left(S_h \left([\![c]\!] + \frac{h}{\lambda} p \right) [\![\theta]\!] + \frac{h}{\lambda} \left(\left([\![c]\!] + \frac{h}{\lambda} p \right) S_h - p \right) \delta p \right) \mathrm{d}\mathit{\Gamma}_*, \tag{68}$$

$$\delta p = \vec{N}_\mathrm{I} \cdot \left\langle \frac{\partial \vec{j}}{\partial \nabla_0 c} \cdot \nabla_0 \theta \right\rangle, \tag{69}$$

where $\theta_\pm = \delta c_\pm$ are the test functions belonging to domains $\mathit{\Omega}_\pm$. Next, the following inter-element stabilisation term is introduced:

$$\begin{aligned} \delta \mathit{\Pi}_\mathrm{I} = & \sum_{\mathit{\Gamma}_\mathrm{f} \in \mathcal{F}_+^*} kh \int_{\mathit{\Gamma}_\mathrm{f}} \left[\!\!\left[\vec{N}_\mathrm{f} \cdot \nabla_0 c_+ \right]\!\!\right]_\mathrm{e} \cdot \left[\!\!\left[\vec{N}_\mathrm{f} \cdot \nabla_0 \theta_+ \right]\!\!\right]_\mathrm{e} \mathrm{d}\mathit{\Gamma}_\mathrm{f} + \\ & + \sum_{\mathit{\Gamma}_\mathrm{f} \in \mathcal{F}_-^*} kh \int_{\mathit{\Gamma}_\mathrm{f}} \left[\!\!\left[\vec{N}_\mathrm{f} \cdot \nabla_0 c_- \right]\!\!\right]_\mathrm{e} \cdot \left[\!\!\left[\vec{N}_\mathrm{f} \cdot \nabla_0 \theta_- \right]\!\!\right]_\mathrm{e} \mathrm{d}\mathit{\Gamma}_\mathrm{f}, \end{aligned} \tag{70}$$

where $\mathcal{F}_\pm^*$ are the sets of element boundaries that belong to the elements covering the interface, the elements, in turn, belong to the meshes covering domains $\mathit{\Omega}_\pm$, respectively. Further details can be found in section 2.5 of reference [49]. Here, $\vec{N}_\mathrm{f}$ is the normal to boundary $\mathit{\Gamma}_\mathrm{f}$, k is the stabilisation parameter and $[\![\cdot]\!]_\mathrm{e}$ denotes the jump of the quantity across the element boundary. Finally, the bulk terms are written as in equation (51),

$$\delta \mathit{\Pi}_\pm = \int_{\mathit{\Omega}_\pm} \left(M_* \dot{c}_\pm \theta_\pm - \vec{j}_\pm \cdot \nabla_0 \theta_\pm - \zeta \omega_\pm \theta_\pm \right) \mathrm{d}\mathit{\Omega}_\pm + \int_{\mathit{\Gamma}_\pm} \vec{N}_\mathit{\Gamma} \cdot \vec{j}_\pm \theta_\pm \, \mathrm{d}\mathit{\Gamma}_\pm = 0, \tag{71}$$

where it is implied that the time derivatives can be handled implicitly or explicitly. Furthermore, the distinction is made between the reaction rates $\omega_\pm$ defined within domains $\mathit{\Omega}_\pm$, respectively. The resulting weak problem formulation consists in finding $c_\pm$, such that

$$\delta \mathit{\Pi}_+ + \delta \mathit{\Pi}_- + \delta \mathit{\Pi}_* + \delta \mathit{\Pi}_\mathrm{I} = 0. \tag{72}$$

for any test functions $\theta_\pm$, where the unknown and the test functions belong to the appropriate functional spaces. It can be seen that this appendix is mainly a simplification of the corresponding section 2.3 of reference [49] for the scalar case, which is, in turn, based on reference [59].

References

[1] A. M. Huntz, G. Calvarin Amiri, H. E. Evans, and G. Cailletaud. Comparison of oxidation-growth stresses in NiO film measured by deflection and calculated using creep analysis or finite-element modeling. *Oxidation of Metals*, 57(5-6):499–521, 2002.

[2] C. C. Büttner and M. Zacharias. Retarded oxidation of Si nanowires. *Applied Physics Letters*, 89(26):263106, 2006.

[3] K. Keune and J. J. Boon. Analytical imaging studies of cross-sections of paintings affected by lead soap aggregate formation. *Studies in Conservation*, 52(3):161–176, 2007.

[4] M. T. McDowell, S. W. Lee, W. D. Nix, and Y. Cui. 25th anniversary article: Understanding the lithiation of silicon and other alloying anodes for lithium-ion batteries. *Advanced Materials*, 25(36):4966–4984, 2013.

[5] C. R. Hickenboth, J. S. Moore, S. R. White, N. R. Sottos, J. Baudry, and S. R. Wilson. Biasing reaction pathways with mechanical force. *Nature*, 446:423–427, 2007.

[6] R. Rana, N. Hopper, F. Sidoroff, and W. T. Tysoe. Critical stresses in mechanochemical reactions. *Chemical Science*, 13:12651–12658, 2022.

[7] K. M. Wiggins, J. N. Brantley, and C. W. Bielawski. Polymer mechanochemistry: Force enabled transformations. *ACS Macro Letters*, 1:623–626, 2012.

[8] H.-A. Klok, A. Herrmann, and R. Göstl. Force ahead: Emerging applications and opportunities of polymer mechanochemistry. *ACS Polymers Au*, 2(4):208–212, 2022.

[9] S. Pagola. Outstanding advantages, current drawbacks, and significant recent developments in mechanochemistry: A perspective view. *Crystals*, 13:124, 2023.

[10] S. S. M. Konda, J. N. Brantley, C. W. Bielawski, and D. E. Makarov. Chemical reactions modulated by mechanical stress: Extended Bell theory. *The Journal of Chemical Physics*, 135(16):164103, 2011.

[11] A. Boscoboinik, D. Olson, H. Adams, N. Hopper, and W. T. Tysoe. Measuring and modelling mechanochemical reaction kinetics. *Chemical Communications*, 56:7730–7733, 2020.

[12] A. Ghasemi and W. Gao. A method to predict energy barriers in stress modulated solid-solid phase transitions. *Journal of the Mechanics and Physics of Solids*, 137:103857, 2020.

[13] S. Walcott. The load dependence of rate constants. *The Journal of Chemical Physics*, 128(21):215101, 2008.

[14] H. Adams, B. P. Miller, O. J. Furlong, M. Fantauzzi, G. Navarra, A. Rossi, Y. Xu, P. V. Kotvis, and W. T. Tysoe. Modeling mechanochemical reaction mechanisms. *ACS Applied Materials and Interfaces*, 9(31):26531–26538, 2017.

[15] M. Alrbaihat, F. K. Al-Zeidaneen, and Q. Abu-Afifeh. Reviews of the kinetics of mechanochemistry: Theoretical and modeling aspects. *Materials Today: Proceedings*, 65:3651–3656, 2022.

[16] P. Glansdorff and I. Prigogine. *Thermodynamic theory of structure, stability and fluctuations.* John Wiley & Sons Ltd, 1971.

[17] K. Loeffel and L. Anand. A chemo-thermo-mechanically coupled theory for elastic-viscoplastic deformation, diffusion, and volumetric swelling due to a chemical reaction. *International Journal of Plasticity*, 27(9):1409–1431, 2011.

[18] A. F. Bower, P. R. Guduru, and V. A. Sethuraman. A finite strain model of stress, diffusion, plastic flow, and electrochemical reactions in a lithium-ion half-cell. *Journal of the Mechanics and Physics of Solids*, 59(4):804–828, 2011.

[19] Z. W. Cui, F. Gao, and J. M. Qu. A finite deformation stress-dependent chemical potential and its applications to lithium ion batteries. *Journal of the Mechanics and Physics of Solids*, 60(7):1280–1295, 2012.

[20] V. I. Levitas and H. Attariani. Anisotropic compositional expansion in elastoplastic materials and corresponding chemical potential: Large-strain formulation and application to amorphous lithiated silicon. *Journal of the Mechanics and Physics of Solids*, 69:84–111, 2014.

[21] A. G. Knyazeva. Cross effects in solid media with diffusion. *Journal of Applied Mechanics and Technical Physics*, 44(3):373–384, 2003.

[22] K. Loeffel, L. Anand, and Z. M. Gasem. On modeling the oxidation of high-temperature alloys. *Acta Materialia*, 61(2):399–424, 2013.

[23] A. D. Drozdov. Viscoplastic response of electrode particles in Li-ion batteries driven by insertion of lithium. *International Journal of Solids and Structures*, 51:690–705, 2014.

[24] V. S. Rao and T. J. R. Hughes. On modelling thermal oxidation of silicon I: Theory. *International Journal for Numerical Methods in Engineering*, 47(1-3):341–358, 2000.

[25] Z. W. Cui, F. Gao, and J. M. Qu. Interface-reaction controlled diffusion in binary solids with applications to lithiation of silicon in lithium-ion batteries. *Journal of the Mechanics and Physics of Solids*, 61(2):293–310, 2013.

[26] A. B. Freidin, E. N. Vilchevskaya, and I. K. Korolev. Stress-assist chemical reactions front propagation in deformable solids. *International Journal of Engineering Science*, 83:57–75, 2014.

[27] A. B. Freidin and E. N. Vilchevskaya. Chemical affinity tensor in coupled problems of mechanochemistry. In H. Altenbach and A. Öchsner, editors, *Encyclopedia of Continuum Mechanics*, pages 264–280. Springer Berlin Heidelberg, 2020.

[28] H.-J. Cheng, X.-C. Zhang, Y.-F. Jia, F. Yang, and S.-T. Tu. A finite element simulation on fully coupled diffusion, stress and chemical reaction. *Mechanics of Materials*, 166:104217, 2022.

[29] B. Qin and Z. Zhong. A theoretical model for thermo-chemo-mechanically coupled problems considering plastic flow at large deformation and its application to metal oxidation. *International Journal of Solids and Structures*, 212:107–123, 2021.

[30] M. G. D. Geers, V. G. Kouznetsova, and W. A. M. Brekelmans. Multi-scale computational homogenization: Trends and challenges. *Journal of Computational and Applied Mathematics*, 234(7):2175–2182, 2010.

[31] J. Yvonnet. *Computational homogenization of heterogeneous materials with finite elements*. Springer Nature Switzerland AG, 2019.

[32] I. Özdemir, W. A. M. Brekelmans, and M. G. D. Geers. Computational homogenization for heat conduction in heterogeneous solids. *International Journal for Numerical Methods in Engineering*, 73(2):185–204, 2008.

[33] I. Özdemir, W. A. M. Brekelmans, and M. G. D. Geers. FE^2 computational homogenization for the thermo-mechanical analysis of heterogeneous solids. *Computer Methods in Applied Mechanics and Engineering*, 198(3-4):602–613, 2008.

[34] A. Salvadori, E. Bosco, and D. Grazioli. A computational homogenization approach for Li-ion battery cells: Part 1 — formulation. *Journal of the Mechanics and Physics of Solids*, 65:114–137, 2014.

[35] A. Salvadori, D. Grazioli, and M. G. D. Geers. Governing equations for a two-scale analysis of Li-ion battery cells. *International Journal of Solids and Structures*, 59:90–109, 2015.

[36] A. Salvadori, R. McMeeking, D. Grazioli, and M. Magri. A coupled model of transport-reaction-mechanics with trapping. Part 1 — Small strain analysis. *Journal of the Mechanics and Physics of Solids*, 114:1–30, 2018.

[37] L. Brassart and L. Stainier. Effective transient behaviour of heterogeneous media in diffusion problems with a large contrast in the phase diffusivities. *Journal of the Mechanics and Physics of Solids*, 124:366–391, 2019.

[38] A. Waseem, T. Heuzé, L. Stainier, M. G. D. Geers, and V. G. Kouznetsova. Enriched continuum for multi-scale transient diffusion coupled to mechanics. *Advanced Modeling and Simulation in Engineering Sciences*, 7(1):14, 2020.

[39] S. Kaessmair, K. Runesson, P. Steinmann, R. Jänicke, and F. Larsson. Variationally consistent computational homogenization of chemomechanical problems with stabilized weakly periodic boundary conditions. *International Journal for Numerical Methods in Engineering*, 122(22):6429–6454, 2021.

[40] M. Poluektov and Ł. Figiel. A numerical method for finite-strain mechanochemistry with localised chemical reactions treated using a Nitsche approach. *Computational Mechanics*, 63(5):885–911, 2019.

[41] X. H. Liu, H. Zheng, L. Zhong, S. Huan, K. Karki, L. Q. Zhang, Y. Liu, A. Kushima, W. T. Liang, J. W. Wang, J. H. Cho, E. Epstein, S. A. Dayeh, S. T. Picraux, T. Zhu, J. Li, J. P. Sullivan, J. Cumings, C. S. Wang, S. X. Mao, Z. Z. Ye, S. L. Zhang, and J. Y. Huang. Anisotropic swelling and fracture of silicon nanowires during lithiation. *Nano Letters*, 11(8):3312–3318, 2011.

[42] T. Belytschko and T. Black. Elastic crack growth in finite elements with minimal remeshing. *International Journal for Numerical Methods in Engineering*, 45(5):601–620, 1999.

[43] N. Moës, J. Dolbow, and T. Belytschko. A finite element method for crack growth without remeshing. *International Journal for Numerical Methods in Engineering*, 46(1):131–150, 1999.

[44] T. Belytschko, R. Gracie, and G. Ventura. A review of extended/generalized finite element methods for material modeling. *Modelling and Simulation in Materials Science and Engineering*, 17(4):043001, 2009.

[45] E. Burman and P. Hansbo. Fictitious domain finite element methods using cut elements: II. A stabilized Nitsche method. *Applied Numerical Mathematics*, 62(4):328–341, 2012.

[46] E. Burman, S. Claus, P. Hansbo, M. G. Larson, and A. Massing. CutFEM: Discretizing geometry and partial differential equations. *International Journal for Numerical Methods in Engineering*, 104(7):472–501, 2015.

[47] P. Hansbo, M. G. Larson, and K. Larsson. Cut finite element methods for linear elasticity problems. In S. P. A. Bordas, E. Burman, M. G. Larson, and M. A. Olshanskii, editors, *Geometrically Unfitted Finite Element Methods and Applications*, pages 25–63. Springer International Publishing, 2017.

[48] A. Hansbo and P. Hansbo. An unfitted finite element method, based on Nitsche's method, for elliptic interface problems. *Computer Methods in Applied Mechanics and Engineering*, 191:5537–5552, 2002.

[49] M. Poluektov and Ł. Figiel. A cut finite-element method for fracture and contact problems in large-deformation solid mechanics. *Computer Methods in Applied Mechanics and Engineering*, 388:114234, 2022.

[50] K. van Havenbergh, S. Turner, N. Marx, and G. van Tendeloo. The mechanical behavior during (de)lithiation of coated silicon nanoparticles as anode material for lithium-ion batteries studied by insitu transmission electron microscopy. *Energy Technology*, 4(8):1005–1012, 2016.

[51] S. Müller, P. Pietsch, B.-E. Brandt, P. Baade, V. De Andrade, F. De Carlo, and V. Wood. Quantification and modeling of mechanical degradation in lithium-ion batteries based on nanoscale imaging. *Nature Communications*, 9(1):2340, 2018.

[52] P. Kumar, C. L. Berhaut, D. Z. Dominguez, E. De Vito, S. Tardif, S. Pouget, S. Lyonnard, and P. H. Jouneau. Nano-architectured composite anode enabling long-term cycling stability for high-capacity lithium-ion batteries. *Small*, 16(11):1906812, 2020.

[53] J. H. Rose, J. Ferrante, and J. R. Smith. Universal binding energy curves for metals and bimetallic interfaces. *Physical Review Letters*, 47(9):675–678, 1981.

[54] T. Kosztołowicz and S. Mrówczyński. Membrane boundary condition. *Acta Physica Polonica B*, 32(1):217–226, 2001.

[55] A. B. Freidin. On the chemical affinity tensor for chemical reactions in deformable materials. *Mechanics of Solids*, 50(3):260–285, 2015.

[56] A. B. Freidin, N. Morozov, S. Petrenko, and E. N. Vilchevskaya. Chemical reactions in spherically symmetric problems of mechanochemistry. *Acta Mechanica*, 227(1):43–56, 2016.

[57] A. B. Freidin, I. K. Korolev, S. P. Aleshchenko, and E. N. Vilchevskaya. Chemical affinity tensor and chemical reaction front propagation: Theory and FE-simulations. *International Journal of Fracture*, 202(2):245–259, 2016.

[58] M. Poluektov, A. B. Freidin, and Ł. Figiel. Modelling stress-affected chemical reactions in non-linear viscoelastic solids with application to lithiation reaction in spherical Si particles. *International Journal of Engineering Science*, 128:44–62, 2018.

[59] A. Hansbo and P. Hansbo. A finite element method for the simulation of strong and weak discontinuities in solid mechanics. *Computer Methods in Applied Mechanics and Engineering*, 193(33-35):3523–3540, 2004.

[60] P. Hansbo. Nitsche's method for interface problems in computational mechanics. *GAMM-Mitteilungen*, 28(2):183–206, 2005.

Highlights

- A general thermodynamically-consistent thermo-chemo-mechanical theory is proposed.
- Computational homogenisation framework is proposed for the theory.
- Chemical reaction locking due to mechanical stresses is modelled.

Declaration of interests

☐ The authors declare that they have no known competing financial interests or personal relationships that could have appeared to influence the work reported in this paper.

☒ The authors declare the following financial interests/personal relationships which may be considered as potential competing interests:

M. Poluektov reports financial support was provided by European Union.